

Controlling surface carrier density by illumination in the transparent conductor La-doped BaSnO₃

Edward B. Lochocki, Hanjong Paik, Masaki Uchida, Darrell G. Schlom, and Kyle M. Shen

Citation: *Appl. Phys. Lett.* **112**, 181603 (2018); doi: 10.1063/1.5020716

View online: <https://doi.org/10.1063/1.5020716>

View Table of Contents: <http://aip.scitation.org/toc/apl/112/18>

Published by the [American Institute of Physics](#)

Articles you may be interested in

[Interface energy band alignment at the all-transparent p-n heterojunction based on NiO and BaSnO₃](#)

Applied Physics Letters **112**, 171605 (2018); 10.1063/1.5029422

[Transition regime from step-flow to step-bunching in the growth of epitaxial SrRuO₃ on \(001\) SrTiO₃](#)

Applied Physics Letters **112**, 182902 (2018); 10.1063/1.5026682

[Oxygen-vacancy-mediated dielectric property in perovskite Eu_{0.5}Ba_{0.5}TiO_{3-δ} epitaxial thin films](#)

Applied Physics Letters **112**, 182906 (2018); 10.1063/1.5025607

[Synthesis science of SrRuO₃ and CaRuO₃ epitaxial films with high residual resistivity ratios](#)

APL Materials **6**, 046101 (2018); 10.1063/1.5023477

[Adsorption-controlled growth of La-doped BaSnO₃ by molecular-beam epitaxy](#)

APL Materials **5**, 116107 (2017); 10.1063/1.5001839

[Stability of the oxygen vacancy induced conductivity in BaSnO₃ thin films on SrTiO₃](#)

Applied Physics Letters **111**, 172102 (2017); 10.1063/1.4996548

PHYSICS TODAY

WHITEPAPERS

MANAGER'S GUIDE

Accelerate R&D with
Multiphysics Simulation

READ NOW

PRESENTED BY

 COMSOL

Controlling surface carrier density by illumination in the transparent conductor La-doped BaSnO₃

Edward B. Lochocki,¹ Hanjong Paik,² Masaki Uchida,³ Darrell G. Schlom,^{2,4} and Kyle M. Shen^{2,4,a)}

¹Laboratory of Atomic and Solid State Physics, Department of Physics, Cornell University, Ithaca, New York 14853, USA

²Department of Materials Science and Engineering, Cornell University, Ithaca, New York 14853, USA

³Department of Applied Physics and Quantum-Phase Electronics Center (QPEC), University of Tokyo, Tokyo 113-8656, Japan

⁴Kavli Institute at Cornell for Nanoscale Science, Ithaca, New York 14853, USA

(Received 26 December 2017; accepted 16 April 2018; published online 3 May 2018)

La_xBa_{1-x}SnO₃ is a promising transparent conducting oxide whose high mobility facilitates potential applications in transparent electronics, oxide electronics, and power electronics. Here, we report quantitative comparisons between angle-resolved photoemission and density functional theory, demonstrating a close agreement between calculations and the measured bulk electronic structure. Further measurements reveal upward band bending at the film-vacuum interface, while ultraviolet (UV) exposure is found to increase the surface electron density, similar to other oxides. These results elucidate the La_xBa_{1-x}SnO₃ (LBSO) interfacial electronic structure and offer a route for UV carrier density control, critical steps towards realizing LBSO-based electronic devices. *Published by AIP Publishing.*

<https://doi.org/10.1063/1.5020716>

Transparent conducting oxides (TCOs) play a crucial role in modern electronic devices such as liquid crystal displays, photovoltaic cells, light-emitting diodes, and future transparent electronics.¹⁻⁴ The central challenge in TCO applications is to maximize the visible light transmission of a thin film while retaining the high conductivity required for low power consumption. The figure of merit σ/α , where σ is the electrical conductivity and α is the absorption coefficient at 550 nm, expresses the ability of a material to perform as a transparent conductor.¹ In single crystals of La_xBa_{1-x}SnO₃ (LBSO), this ratio has been shown to exceed $30 \Omega^{-1}$,⁵ significantly improving upon traditional TCOs such as indium tin oxide ($\sigma/\alpha \approx 1 \Omega^{-1}$),⁶ CdO ($\sigma/\alpha \approx 3 \Omega^{-1}$),⁷ and Cd₂SnO₄ ($\sigma/\alpha \approx 7 \Omega^{-1}$).¹ This remarkable performance, driven by a room temperature mobility of $320 \text{ cm}^2 \text{ V}^{-1} \text{ s}^{-1}$ and a wide bandgap of $\sim 3.1 \text{ eV}$, has generated great interest in LBSO as a promising TCO and high mobility oxide.⁸⁻¹¹ BaSnO₃ (BSO) has also been investigated as a host for interfacial electron gases^{12,13} and *p-n* junctions.¹⁴ Furthermore, BSO adopts the same perovskite structure as complex oxides such as SrRuO₃ and La_{1-x}Sr_xMnO₃, many of which exhibit exotic electronic and magnetic properties including exotic superconductivity and colossal magnetoresistance.¹⁵ This shared crystal structure suggests the possibility of epitaxially integrating BSO into next-generation oxide-based devices that could possess an unprecedented range of electronic and magnetic functionalities.^{16,17}

Understanding both the bulk and interfacial electronic structures of LBSO is crucial for device applications, since most promising devices involve heterostructures. Investigating the electronic response of LBSO to photons with energies above the bandgap is also key for implementing LBSO as a TCO. Here, we report the electronic structure of LBSO thin films synthesized by molecular-beam epitaxy (MBE). *In situ*

angle-resolved photoemission spectroscopy (ARPES) measurements reveal that the occupied electronic structure of LBSO is well described by density functional theory (DFT) calculations of the valence band, while charged defects induce upward band bending at the LBSO surface. Furthermore, we demonstrate that the surface electron concentration can be controlled by ultraviolet (UV) exposure, suggesting that band offsets and transport properties at LBSO interfaces can be modified by illumination.

Cubic perovskite LBSO films [see Fig. 1(a)] with thicknesses of 10–30 nm were grown by adsorption controlled oxide MBE, where La concentrations ranging from 1 to 10% were achieved by codepositing La, Ba, and Sn.¹⁸ The films were deposited on TbScO₃ and GdScO₃ substrates (3.8% and 3.6% compressive strain, respectively). The lattice mismatch for LBSO on TbScO₃ or GdScO₃ is smaller than for LBSO on SrTiO₃ (5.1% compressive strain), and the films exhibit room temperature mobilities and resistivities between 20 and $140 \text{ cm}^2 \text{ V}^{-1} \text{ s}^{-1}$ and 0.5 and 2.0 m Ω cm, respectively [see Figs. 1(c)–1(d)]. However, typical low-energy electron diffraction (LEED) measurements reveal a surface lattice constant of $4.15 \pm 0.08 \text{ \AA}$, indicating that the films are fully relaxed. Following growth, *in situ* ARPES and LEED measurements were made at temperatures ranging from 15 to 300 K and pressures below 1×10^{-10} Torr. *Ab initio* band structure calculations were performed using the WIEN2k DFT software package,¹⁹ where the exchange-correlation functional was approximated using the Perdew-Burke-Ernzerhof implementation of the generalized gradient method²⁰ and spin orbit coupling was included. The experimental lattice constant of 4.116 \AA was used without any structural relaxation, and the shifted k-mesh included $27 \times 27 \times 27$ points in the full zone. The product of the smallest muffin-tin radius (1.79 Bohr, for O) and the largest K-vector of the plane wave expansion was fixed to be $RK_{\text{max}} = 8.0$.

^{a)}Author to whom correspondence should be addressed: kmschen@cornell.edu

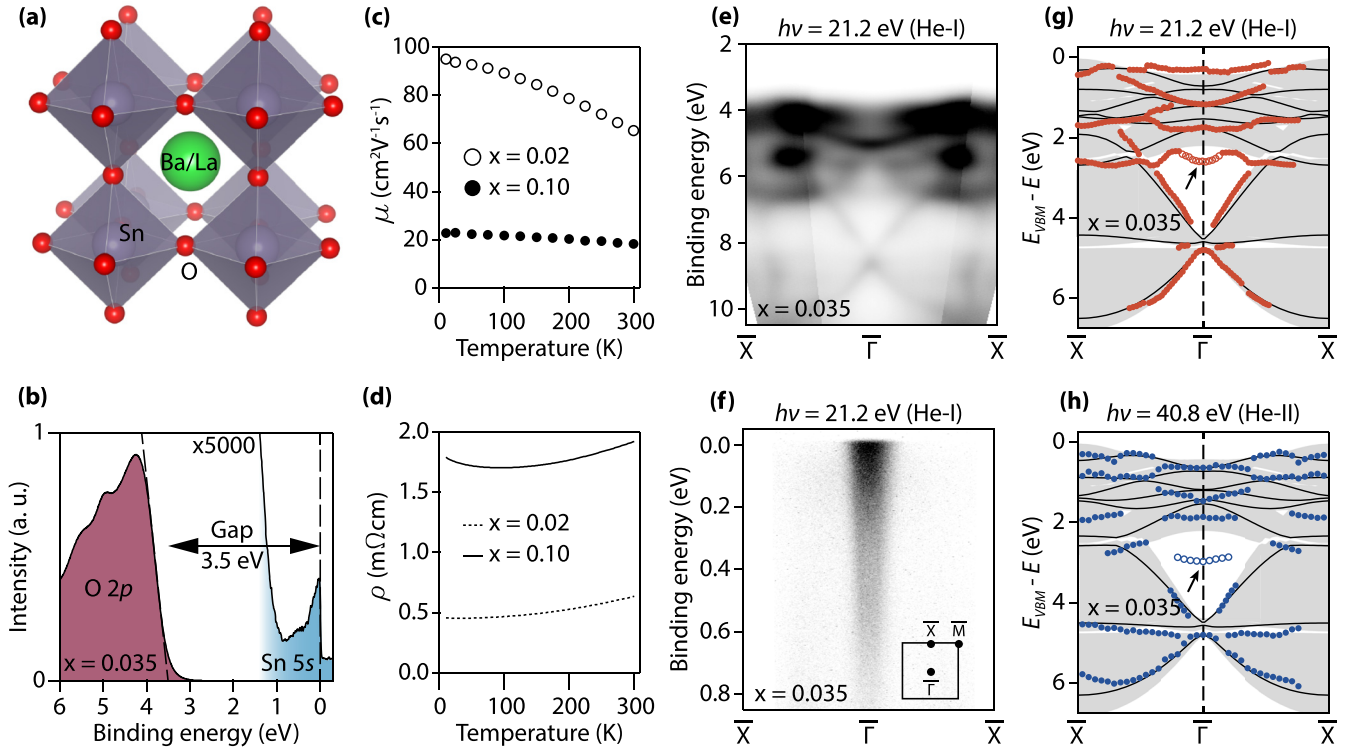


FIG. 1. Overview of LBSO films and their electronic structure. (a) Crystal structure of the cubic perovskite LBSO. (b) Angle-integrated He I photoemission intensity. (c) and (d) Mobility and resistivity measured as a function of temperature from two LBSO films. (e) and (f) ARPES spectra measured from LBSO with He I light ($h\nu = 21.2$ eV) along the $k_x = 0$ line of the SBZ showing (e) the valence bands and (f) a metallic state near E_F . The inset in (f) shows the SBZ. (g) and (h) Comparison of the DFT band structure to extracted valence band dispersions measured along $k_x = 0$ with (g) He I and (h) He II ($h\nu = 40.8$ eV). The projected bulk band structure is shown in gray, and error bars are comparable to the symbol size. The energy resolution for He I (He II) ARPES measurements is $\Delta E = 10$ meV ($\Delta E = 40$ meV).

Figure 1(e) shows typical ARPES spectra from $\text{La}_{0.035}\text{Ba}_{0.965}\text{SnO}_3$ measured along the $k_x = 0$ direction of the surface Brillouin zone (SBZ). Highly dispersive bands are observed for binding energies ranging from 4 to 10 eV, with a dramatic drop in intensity at 3.5 eV [see Fig. 1(b)], which we determine to be the valence band maximum (VBM). Previous LBSO studies have reported optical gaps between 2.85 and 4.02 eV,^{21–25} indicating that the chemical potential in $\text{La}_{0.035}\text{Ba}_{0.965}\text{SnO}_3$ has been pushed upwards near the BSO conduction band minimum (CBM) consistent with electron doping and previous ARPES measurements.²⁶ All samples exhibit a metallic state crossing the Fermi level (E_F) near $(k_x, k_y) = (0, 0)$, as shown in Fig. 1(f) for the sample with $x = 0.035$.

While many proposed applications of LBSO have been based on DFT calculations of its band structure, the agreement between theory and experiment has yet to explicitly be verified. Here, we perform a direct comparison between DFT calculations for the valence band of undoped bulk BSO with the experimental dispersion of occupied states as measured by ARPES. Figures 1(g)–1(h) show band positions extracted from the ARPES spectra by fits to peaks in the energy distribution curves (EDCs), using both He I ($h\nu = 21.2$ eV) and He II ($h\nu = 40.8$ eV) photons, which measure different out-of-plane momenta k_z . By matching the DFT band structure along the $(k_x = 0, k_y)$ line to the highly dispersive bands that lie 3 eV below the VBM, the k_z values for He I and He II photons are determined to be $k_z = 3.4$ and $4.5 \pi/a$, respectively, corresponding to an inner potential of $V_0 = 17$ eV.

Figures 1(g) and 1(h) also show a full comparison between the experimental data and the DFT calculations using a rigid shift of the chemical potential. The ARPES data closely match the DFT band structure, including the overall bandwidth, indicating that DFT accurately treats the bulk BSO electronic structure (notwithstanding the value of the bandgap). This good agreement confirms the general validity of using DFT-based approaches for studying BSO valence bands.

Additional features are also apparent in the ARPES spectra that do not correspond to bands in the bulk DFT calculations for any k_z value [marked as open symbols in Figs. 1(g) and 1(h)], which may be attributed to defects or surface states. In other TCOs such as CdO and In_2O_3 , surface states and native defects typically act as donors, resulting in downward band bending and electron accumulation layers at the surfaces of n -type materials.^{27,28} It has been argued that the characteristic n -type TCO band structure generally favors surface Fermi level pinning above the CBM.^{4,29} Since most proposed applications involving LBSO rely on its interfacial electronic structure, the presence of band bending and surface defect states may have significant consequences for device design and performance.

In Fig. 2, a series of films with different La contents are investigated which clearly demonstrate that LBSO surfaces exhibit band bending. The addition of electrons to a semiconductor shifts the Fermi level upward, causing the valence and conduction band binding energies to increase, as observed in LBSO by bulk-sensitive hard x-ray photoemission spectroscopy

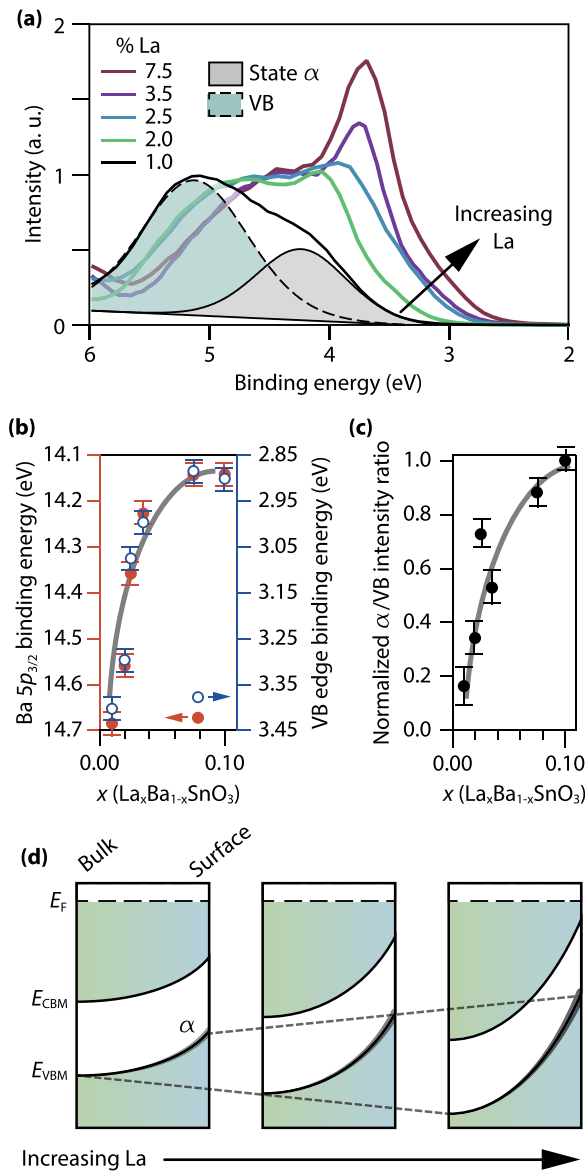


FIG. 2. Upward band bending in LBSO films. (a) EDCs measured near $(k_x, k_y) = (0,0)$ with He II for samples with different La contents; the energy resolution is $\Delta E = 40$ meV. (b) and (c) Ba $5p_{3/2}$ binding energy, valence band edge binding energy, and normalized α /valence band intensity ratio as a function of La content. Lines are guides to the eye. (d) Schematic diagram illustrating band positions and the α state intensity at the surface and bulk for different La concentrations.

(HAXPES).³⁰ In Fig. 2(a), a series of EDCs are shown from near $(k_x, k_y) = (0,0)$ for several different films, where each EDC was measured immediately after transferring the film to the ARPES chamber without exposing it to air. In contrast to the HAXPES results, the VB and core levels are observed to shift towards smaller binding energies as the La concentration increases from 1% to 10% [Fig. 2(b)], counter to expectations from a simple rigid-band electron doping model. Due to the surface sensitivity of ARPES, this opposite trend indicates an opposite evolution of the chemical potential of the surface and bulk, suggesting upwards band bending [Fig. 2(d)].

In addition to the decrease in binding energy, the intensity of a peak in the valence band (labeled α) increases with doping [Fig. 2(c)], which we attribute to oxygen adsorption as reported in other oxides such as SrTiO_3 and CaVO_3 .^{31,32} Based on the dependence of the intensity of α with the La

content, La dopants in LBSO may affect the density of surface oxygen adsorbates in addition to the bulk carrier density, influencing the degree of surface band bending and indicating a complex interplay between defects at the LBSO surface.

The observed band bending likely reflects different defect energetics at the surface versus the bulk, which could impact future devices that utilize LBSO, e.g., transparent electronics in photovoltaics.³³ In other oxides such as SrTiO_3 , KTaO_3 , and SrVO_3 , exposure to high intensity UV photons induces a surface two-dimensional electron gas (2DEG), where the increase in electron density is attributed to the removal of oxygen from the surface.^{34–36} In BSO, UV exposure has been found to induce a 10^7 -fold increase in conductivity that decays on a timescale of hours after the light is removed,³⁷ but the role of the surface in this persistent photoconductivity has not been explored.

The electronic structure of LBSO was tracked over the course of illumination with a helium lamp ($\sim 9 \times 10^{11}$ photons/s using He I, $\sim 2 \times 10^{10}$ photons/s using He II).³⁸ Figure 3(a) shows measurements of $\text{La}_{0.035}\text{Ba}_{0.965}\text{SnO}_3$ near $(k_x, k_y) = (0,0)$

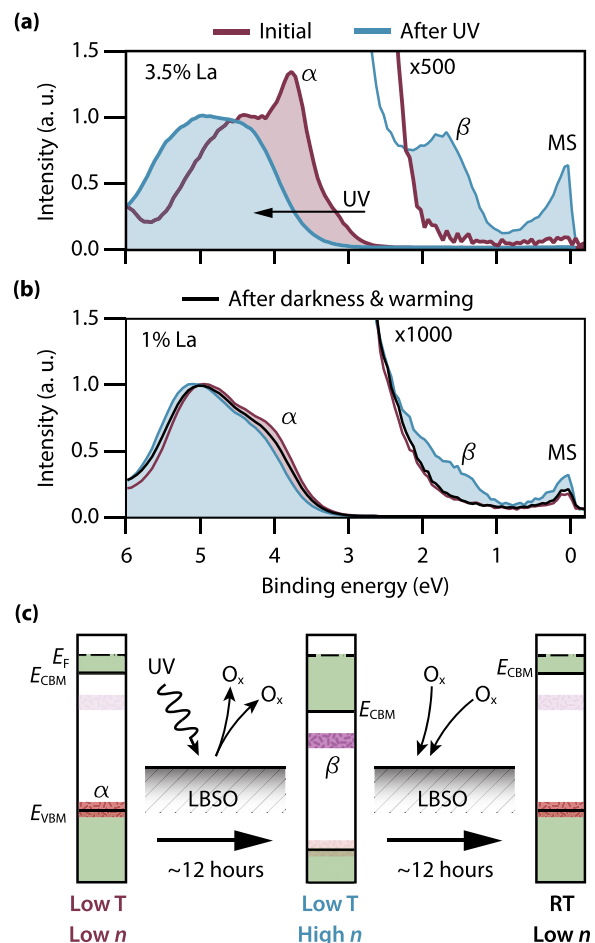


FIG. 3. Response of LBSO films to UV light. (a) and (b) EDCs measured near $(k_x, k_y) = (0,0)$ with He II. (a) EDCs measured from $\text{La}_{0.035}\text{Ba}_{0.965}\text{SnO}_3$ after 10 min and 15 h of UV exposure at low temperature; the energy resolution is $\Delta E = 40$ meV. (b) EDCs measured from $\text{La}_{0.035}\text{Ba}_{0.965}\text{SnO}_3$ after 1 h and 14 h of UV exposure at low temperature and after warming to room temperature in darkness for 12 h; the energy resolution is $\Delta E = 75$ meV. (c) Schematic diagram illustrating the changes in band binding energy, defect state intensities, and surface electron concentration that occur during UV exposure at low temperature and their subsequent reversal while warming in darkness.

made with He II photons at low temperature (~ 30 K). In the first 10 min of UV exposure, the metallic state intensity is negligible, confirming that the bands initially bend upward at the surface. After 15 h of illumination by both He I and He II light ($\sim 7 \times 10^{12}$ photons), several changes occur: (1) the metallic state intensity increases dramatically, (2) the valence band shifts nearly 1 eV towards higher binding energies, (3) the α peak intensity decreases dramatically, and (4) an additional defect state (labeled β) is observed deep within the gap at 1.77 eV. Nevertheless, the spectral features do not become broader, suggesting that these effects are unrelated to degradation. The increase in the intensity of the metallic state indicates that an increase in the surface electron concentration is also responsible for the downward shift observed in the valence band. In Fig. 3(b), a $\text{La}_{0.01}\text{Ba}_{0.99}\text{SnO}_3$ film displays similar changes after receiving $\sim 4 \times 10^{12}$ photons, albeit on a smaller scale, where it is also shown that the changes can be reversed by slowly warming the sample to room temperature in the dark over the course of 12 h.

Figure 3(c) summarizes the UV-induced effects. Initially, the Fermi level near the surface is close to the CBM as a result of the upward band bending, corresponding to a small surface electron concentration. Upon UV exposure, adsorbed oxygen is removed while other defects, likely oxygen vacancies in analogy to SrTiO_3 and KTaO_3 , become apparent, as evidenced by the decrease in the α peak and the simultaneous increase in the β peak. This altered defect population increases the surface electron density and pushes the bands downwards relative to the Fermi level. Upon removing the UV illumination and warming the sample to room temperature over the course of 12 h, the defects return to their original state and the surface electron concentration decreases back to its original value. This may be caused by adsorption of residual O_2 in the vacuum chamber. UV-induced changes to the electronic structure may prove to be a challenge in future devices. On the other hand, this also suggests that careful UV exposure could be a possible route for tailoring the band offsets and electron densities at interfaces between LBSO and other materials in a laboratory setting.

In summary, we have revealed the bulk and surface electronic structure of the TCO LBSO. In contrast to other TCOs, upward band bending is observed at the vacuum interface, and the data indicate a scenario where an increased La content in LBSO films increases both the degree of upward band bending and the adsorbed oxygen concentration at the surface. Subsequent UV exposure removes the adsorbed oxygen, revealing oxygen vacancies that increase the surface carrier concentration. Significant quantities of oxygen vacancies at the surface may form an impurity band that interacts with the bulk conduction band, explaining the appearance of the metallic state. However, despite the peculiarities of defects at the surface, the LBSO valence band is well-reproduced by bulk DFT calculations. These results validate the agreement between DFT calculations for the valence band and ARPES experiments, which may be helpful for designing devices based on LBSO, as well as offer a route for controlling the surface electron concentration and band offsets with other materials through careful UV exposure.

We would like to thank Phil King, Luca Moreschini, and Jisung Park for helpful discussions. This work was supported by the National Science Foundation through the Platform for the Accelerated Realization, Analysis, and Discovery of Interface Materials (PARADIM; DMR-1539918). This research also utilized shared facilities supported by the Cornell Center for Materials Research through the MRSEC program (NSF DMR-1120296) and the Cornell Nanoscale Facility (Grant No. EECs-1542081), a member of the National Nanotechnology Coordinated Infrastructure. We also acknowledge support from the Air Force Office of Scientific Research under Award No. FA9550-16-1-0192.

- ¹G. Haacke, *Annu. Rev. Mater. Sci.* **7**, 73 (1977).
- ²D. S. Ginley and C. Bright, *MRS Bull.* **25**, 15 (2000).
- ³E. Fortunato, D. Ginley, H. Hosono, and D. C. Paine, *MRS Bull.* **32**, 242 (2007).
- ⁴P. D. C. King and T. D. Veal, *J. Phys. Condens. Matter* **23**, 334214 (2011).
- ⁵H. J. Kim, U. Kim, H. M. Kim, T. H. Kim, H. S. Mun, B.-G. Jeon, K. T. Hong, W.-J. Lee, C. Ju, K. H. Kim, and K. Char, *Appl. Phys. Express* **5**, 061102 (2012).
- ⁶H. Kim, C. M. Gilmore, A. Piqué, J. S. Horwitz, H. Mattoussi, H. Murata, Z. H. Kafafi, and D. B. Chrisey, *J. Appl. Phys.* **86**, 6451 (1999).
- ⁷A. Wang, J. R. Babcock, N. L. Edleman, A. W. Metz, M. A. Lane, R. Asahi, V. P. Dravid, C. R. Kannewurf, A. J. Freeman, and T. J. Marks, *Proc. Natl. Acad. Sci.* **98**, 7113 (2001).
- ⁸S. Ismail-Beigi, F. J. Walker, S.-W. Cheong, K. M. Rabe, and C. H. Ahn, *APL Mater.* **3**, 062510 (2015).
- ⁹U. Kim, C. Park, T. Ha, Y. M. Kim, N. Kim, C. Ju, J. Park, J. Yu, J. H. Kim, and K. Char, *APL Mater.* **3**, 036101 (2015).
- ¹⁰K. Krishnaswamy, L. Bjaalie, B. Himmetoglu, A. Janotti, L. Gordon, and C. G. V. de Walle, *Appl. Phys. Lett.* **108**, 083501 (2016).
- ¹¹A. Prakash, P. Xu, A. Faghaninia, S. Shukla, J. W. A. Iii, C. S. Lo, and B. Jalan, *Nat. Commun.* **8**, 15167 (2017).
- ¹²X. Fan, W. Zheng, X. Chen, and D. J. Singh, *PLoS One* **9**, e91423 (2014).
- ¹³U. Kim, C. Park, Y. M. Kim, J. Shin, and K. Char, *APL Mater.* **4**, 071102 (2016).
- ¹⁴H. M. Kim, U. Kim, C. Park, H. Kwon, and K. Char, *APL Mater.* **4**, 056105 (2016).
- ¹⁵E. Dagotto, *Science* **309**, 257 (2005).
- ¹⁶J. Mannhart and D. G. Schlom, *Science* **327**, 1607 (2010).
- ¹⁷H. Y. Hwang, Y. Iwasa, M. Kawasaki, B. Keimer, N. Nagaosa, and Y. Tokura, *Nat. Mater.* **11**, 103 (2012).
- ¹⁸H. Paik, Z. Chen, E. Lochocki, A. Seidner, H. A. Verma, N. Tanen, J. Park, M. Uchida, S. Shang, B.-C. Zhou, M. Brützmam, R. Uecker, Z.-K. Liu, D. Jena, K. M. Shen, D. A. Muller, and D. G. Schlom, *APL Mater.* **5**, 116107 (2017).
- ¹⁹P. Blaha, K. Schwarz, G. K. H. Madsen, D. Kvasnicka, and J. Luitz, *WIEN2K, an Augmented Plane Wave+Local Orbitals Program for Calculating Crystal Properties* (Karlheinz Schwarz, Techn. Universität Wien, Austria, 2001).
- ²⁰J. P. Perdew, K. Burke, and M. Ernzerhof, *Phys. Rev. Lett.* **77**, 3865 (1996).
- ²¹H. Mizoguchi, H. W. Eng, and P. M. Woodward, *Inorg. Chem.* **43**, 1667 (2004).
- ²²B. Hadjarab, A. Bouguelia, and M. Trari, *J. Phys. Appl. Phys.* **40**, 5833 (2007).
- ²³H. F. Wang, Q. Z. Liu, F. Chen, G. Y. Gao, W. Wu, and X. H. Chen, *J. Appl. Phys.* **101**, 106105 (2007).
- ²⁴Q. Liu, J. Liu, B. Li, H. Li, G. Zhu, K. Dai, Z. Liu, P. Zhang, and J. Dai, *Appl. Phys. Lett.* **101**, 241901 (2012).
- ²⁵D. Seo, K. Yu, Y. J. Chang, E. Sohn, K. H. Kim, and E. J. Choi, *Appl. Phys. Lett.* **104**, 022102 (2014).
- ²⁶B. S. Joo, Y. J. Chang, L. Moreschini, A. Bostwick, E. Rotenberg, and M. Han, *Curr. Appl. Phys.* **17**, 595 (2017).
- ²⁷P. D. C. King, T. D. Veal, D. J. Payne, A. Bourlange, R. G. Egdell, and C. F. McConville, *Phys. Rev. Lett.* **101**, 116808 (2008).
- ²⁸P. D. C. King, T. D. Veal, F. Fuchs, C. Y. Wang, D. J. Payne, A. Bourlange, H. Zhang, G. R. Bell, V. Cimalla, O. Ambacher, R. G. Egdell, F. Bechstedt, and C. F. McConville, *Phys. Rev. B* **79**, 205211 (2009).

- ²⁹P. D. C. King, T. D. Veal, P. H. Jefferson, J. Zúñiga-Pérez, V. Muñoz-Sanjosé, and C. F. McConville, *Phys. Rev. B* **79**, 035203 (2009).
- ³⁰Z. Lebens-Higgins, D. O. Scanlon, H. Paik, S. Sallis, Y. Nie, M. Uchida, N. F. Quackenbush, M. J. Wahila, G. E. Sterbinsky, D. A. Arena, J. C. Woicik, D. G. Schlom, and L. F. J. Piper, *Phys. Rev. Lett.* **116**, 027602 (2016).
- ³¹Y. Aiura, H. Kawanaka, H. Bando, and T. Yasue, *Surf. Sci.* **492**, 249 (2001).
- ³²Y. Aiura, I. Hase, H. Bando, T. Yasue, T. Saitoh, and D. S. Dessau, *Surf. Sci.* **515**, 61 (2002).
- ³³S. S. Shin, E. J. Yeom, W. S. Yang, S. Hur, M. G. Kim, J. Im, J. Seo, J. H. Noh, and S. I. Seok, *Science* **356**, 167 (2017).
- ³⁴W. Meevasana, P. D. C. King, R. H. He, S.-K. Mo, M. Hashimoto, A. Tamai, P. Songsiriritthigul, F. Baumberger, and Z.-X. Shen, *Nat. Mater.* **10**, 114 (2011).
- ³⁵P. King, R. He, T. Eknapakul, P. Buaphet, S.-K. Mo, Y. Kaneko, S. Harashima, Y. Hikita, M. Bahramy, C. Bell, Z. Hussain, Y. Tokura, Z.-X. Shen, H. Hwang, F. Baumberger, and W. Meevasana, *Phys. Rev. Lett.* **108**, 117602 (2012).
- ³⁶S. Backes, T. C. Rödel, F. Fortuna, E. Frantzeskakis, P. Le Fèvre, F. Bertran, M. Kobayashi, R. Yukawa, T. Mitsuhashi, M. Kitamura, K. Horiba, H. Kumigashira, R. Saint-Martin, A. Fouchet, B. Berini, Y. Dumont, A. J. Kim, F. Lechermann, H. O. Jeschke, M. J. Rozenberg, R. Valentí, and A. F. Santander-Syro, *Phys. Rev. B* **94**, 241110 (2016).
- ³⁷J. Park, U. Kim, and K. Char, *Appl. Phys. Lett.* **108**, 092106 (2016).
- ³⁸J. W. Harter, P. D. C. King, E. J. Monkman, D. E. Shai, Y. Nie, M. Uchida, B. Burganov, S. Chatterjee, and K. M. Shen, *Rev. Sci. Instrum.* **83**, 113103 (2012).